

# Achieving 2.7 GPa tensile strength in ultrastrong high-carbon steel through prolonged low-temperature tempering

Jian Wang <sup>a,b</sup>, G.M.A.M. El-Fallah <sup>c,\*</sup>, Xiangdong Chang <sup>a</sup>, Yuxing Peng <sup>a</sup>, Qing Tao <sup>b,\*</sup>

<sup>a</sup> School of Mechanical and Electrical Engineering, China University of Mining and Technology, China

<sup>b</sup> School of Materials and Physics, China University of Mining and Technology, China

<sup>c</sup> School of Engineering, University of Leicester, UK

## ARTICLE INFO

### Keywords:

High-carbon steel  
Mechanical properties  
Ultralong-term low-temperature tempering  
Martensite  
Carbide precipitation

## ABSTRACT

The mechanical properties of high-carbon martensitic steel are improved by low-temperature tempering. This is due to carbon diffusion and carbide precipitation, which depend on temperature and time. To further improve mechanical properties and develop optimum tempering conditions of the conventional high-carbon martensitic steel, long-term tempering was carried out at approximately 175 °C and 250 °C. Excellent mechanical properties, which had not been achieved before, were obtained after tempering samples at 175 °C for over 40 d, resulting in tensile strength of 2.7 GPa, yield strength of 2.3 GPa and total strain of 2.6%. Similarly, yield strength values exceeding 2.4 GPa were observed in samples tempered at 250 °C for 5 d. To understand the remarkable outcomes achieved, a detailed investigation into the tempering stages, with the use of Transmission Electron Microscopy (TEM), Scanning Electron Microscopy (SEM), and X-ray Diffraction (XRD) analyses, was essential. The microstructure contained the typical tempered martensite matrix embedded by ultrafine carbides and retained austenite which decomposed slowly with increasing tempering time at 175 °C, contributing to a noticeable increase in strength. Conversely, no pronounced effect of retained austenite was observed on the strength evolution of tempered specimens at 250 °C. At the initial stage of long-term tempering, the primary strengthening mechanism was carbon solid solution strengthening with a value exceeding 1000 MPa. The solid solution strengthening weakened with tempering time, while precipitation strengthening increased with the growth and increasing volume fraction of carbides. The interplay of their effects and the softening of retained austenite led to a trend in which the total yield strength increased, followed by a decrease with increasing holding time. The resulting nuanced mechanical properties and microstructure obtained from long-term tempering offer strategies for synergistic strengthening and ductility of high-carbon steels, thereby facilitating the expansion of their potential applications.

## 1. Introduction

High-carbon martensite steels have been widely used in tooling and bearing applications for several decades due to their strength and wear resistance [1–4]. Increasing the carbon content to about 1 wt%, enhanced strength of plain carbon steel can be obtained by high carbon solid solution strengthening [5]. However, less ductility is compromised in high-carbon martensite [1,6], which has promoted scientists and engineers to explore various approaches for better mechanical properties. Typical carbide precipitation [7–10] and retained austenite (RA) decomposition [9,11–14] at low temperatures are two main conventional fields to release the strength-ductility trade-off.

Barrow et al. [1] have reported the effect of different carbides on the mechanical properties of low-temperature tempered martensite. It is possible to enhance the ductility of high-carbon martensite steel to about 1–2% with 2 GPa tensile strength. Recent research [8,15–17] has shown the atomic-scale analyzed results for carbon clusters and coherent carbides ( $\epsilon$ -,  $\eta$ -carbides) in tempered martensite matrix. Furthermore, the precipitation of carbides is also demonstrated by the predicted modeling in the works of Enrique et al. [18] providing a novel explanation of strength evolution based on dislocation and precipitation strengthening. The precipitation of carbides still means the diluted carbon in the martensite, weakening the solid soliton strengthening [19]. Thus, it allows further tuning of the strengthening and ductility by

\* Corresponding authors.

E-mail addresses: [gmae2@leicester.ac.uk](mailto:gmae2@leicester.ac.uk) (G.M.A.M. El-Fallah), [taoqingyoyo@cumt.edu.cn](mailto:taoqingyoyo@cumt.edu.cn) (Q. Tao).

accurately regulating carbon content in tempered martensite matrix.

Conversely, RA has long been considered a detrimental phase [20] due to its thermodynamic and mechanical instability [21,22], which can compromise the dimensional accuracy of components. The RA can be controlled by cold treatment or tempering [9]. Contradictory findings abound; Qin et al. [23–25] reported high ductility in several high-carbon quenching–partitioning–tempering martensitic steels, including about 30 vol% RA, attributed to the transformation-induced plasticity effect. The carbon partitioning from martensite has been proven effective in enhancing RA stability [26]. However, it is widely acknowledged that increasing tempering temperature accelerates the decomposition of RA [11–13], thereby implying variations in both strength and ductility.

The decomposition of RA in conventional quenched high-carbon steel can also be controlled by the tempering parameters, as well as the carbides precipitation, as mentioned above. A tempering time may exist during which conventional high-carbon steel exhibits excellent mechanical properties. This study performed a prolonged tempering regime on as-quenched high-carbon steel at just 175 °C to determine the optimal tempering time. As a comparative measure, identical steel was tempered at 250 °C. The mechanical properties and microstructural evolution were systematically investigated, with an additional analysis of the strengthening mechanism.

## 2. Experiments and methods

As shown in Fig. 1, a hot rolled high-carbon steel, Fe-1C-1.5Cr-0.6Si-1.1Mn in wt%, was reheated at 1000 °C for 2 h, followed by air cooling to 950 °C and oil quenching to room temperature. Consistent with the bearing manufacturer, the spheroidizing annealing was carried out at 780 °C for 40 min, followed by furnace cooling to 650 °C, and then air cooling to room temperature. After the spheroidizing anneal, large amounts of primary carbides precipitate in the ferrite matrix. Then, the sample was reheated at 840 °C for 1 h, and the oil quenching was carried out. The quenched bulk sample (marked as Q) was cut into thin plates, which were tempered at 175 °C for 0.5 d, 1 d, 5 d, 10 d, 20 d, 40 d, and 80 d. The corresponding specimens were designated as T175°C-0.5D, T175°C-1D, T175°C-5D, T175°C-10D, T175°C—20D, T175°C-40D and T175°C-80D. For comparison, tempering at 250 °C was carried out for 0.5 d, 1 d, 5 d, 10 d, and 20 d (T250°C-0.5D, T250°C-1D, T250°C-5D, T250°C-10D and T250°C-20D).

The microstructure and phase distribution were examined using scanning electron microscopy (SEM, JEOL-7800F) and X-ray diffraction (XRD, Shimadzu 6000, Cu K $\alpha$ , 2°/min) instrument. The specimens for SEM measurement were etched by a solution consisting of 96 ml ethanol and 4 ml HNO<sub>3</sub>. Detailed microstructure of martensite and tempered martensite were characterized using transmission electron microscopy (TEM, JEM 2100F). The foils for TEM were polished using a twin-jet electrochemical method in an ethanol electrolyte with 6 vol%

perchloric acid at –20 °C. The micro-hardness was measured by Vickers hardness tests using a load of 10 N. The hardness values were obtained by taking an average of more than 5 measurements. A uniaxial tensile test was conducted on a Zwick/Roell Z100 testing instrument with a sample gauge of 10 mm × 2 mm at a strain rate of  $1 \times 10^{-3}$  s<sup>-1</sup> at room temperature. To calculate the error, approximately three samples under the same heat treatment were prepared for the tensile test.

## 3. Results

### 3.1. Mechanical properties

The evolution of the mechanical properties of tempered high-carbon steel at 175 °C for varying times was investigated and presented in Fig. 2. A yield strength (YS) of 2346 MPa and ultimate tensile strength (UTS) of 2715 MPa were achieved in the tempered specimen at 175 °C for 40 d, Fig. 2c. With an increase in tempering time from 0.5 d to 40 d, both the YS and UTS experienced a pronounced increase. The total strain of about 2.9% is achieved after tempering for 10 d, which can be attributed to the quenched stress relief and dislocation recovery in the quenched martensite and RA during the initial stages of tempering. However, with an increase in tempering time to 40 d, the decomposition of RA became the primary factor affecting ductility, resulting in a decrease in total strain to about 2.6%. Interestingly, a second increase in total strain was observed after tempering for 80 d, attributed to the exsolution of more carbon atoms from the martensite matrix. Moreover, the enhanced ductility made it possible to obtain a UTS of 2721 MPa after tempering for 80 d, which might be due to more feasible dislocations hardening under the tensile test.

The effect of temperature on carbon exsolution and RA decomposition was investigated by conducting tempering at 250 °C, and the corresponding evolution of strength and ductility is presented in Fig. 3. RA decomposition was significantly accelerated at 250 °C, and primary strengthening effects after long-term tempering included carbide precipitation and solid solution. The maximum YS of 2426 MPa was obtained after tempering at 250 °C for 5 d, Fig. 3c, which was about 80 MPa higher than the maximum YS at 175 °C. Excluding the effect of RA, this extra strength is mainly attributed to the difference in carbon solid solution in the tempered martensite matrix, which will be discussed in detail in section 4. However, the loss of ductility during the first stage of tempering at 250 °C (from 0.5 d to 5 d) suggests that the strengthening effect of carbide precipitation increases with increasing particle size. The weakening of the carbon solid solution strengthening becomes the primary factor during the second stage of tempering (5 d to 20 d), resulting in a lower YS of 2267 MPa. The corresponding total strain increases to 3%. Similar to the results obtained at 175 °C, the maximum UTS of 2583 MPa was observed after tempering at 250 °C for 10 d, attributed to the production of more feasible dislocations hardening.

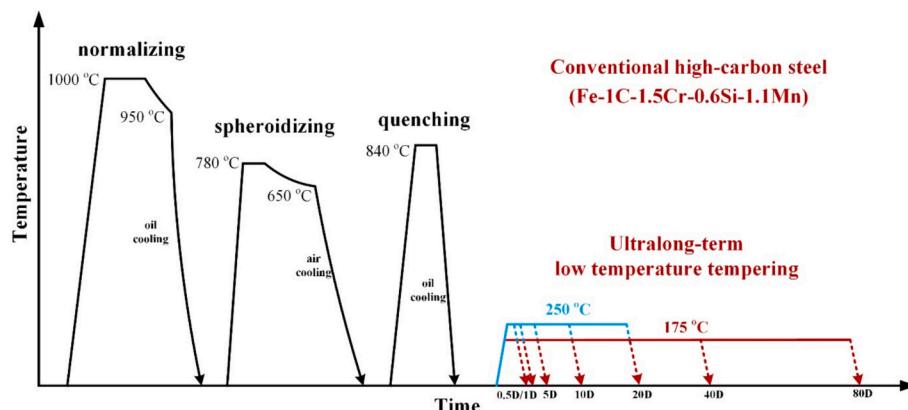
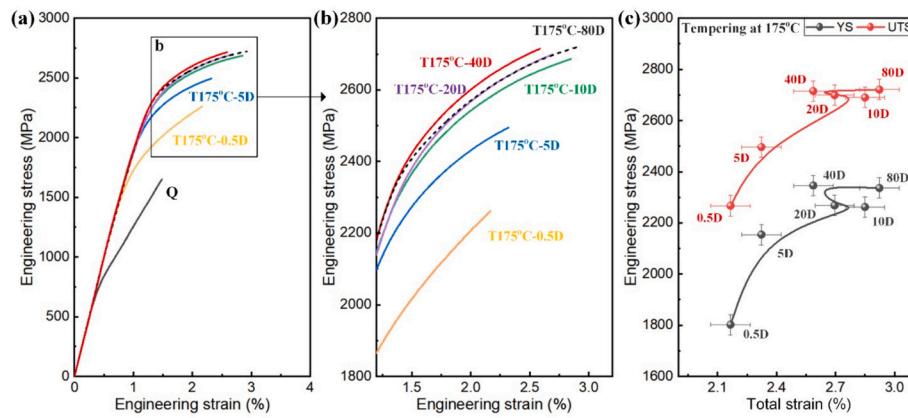
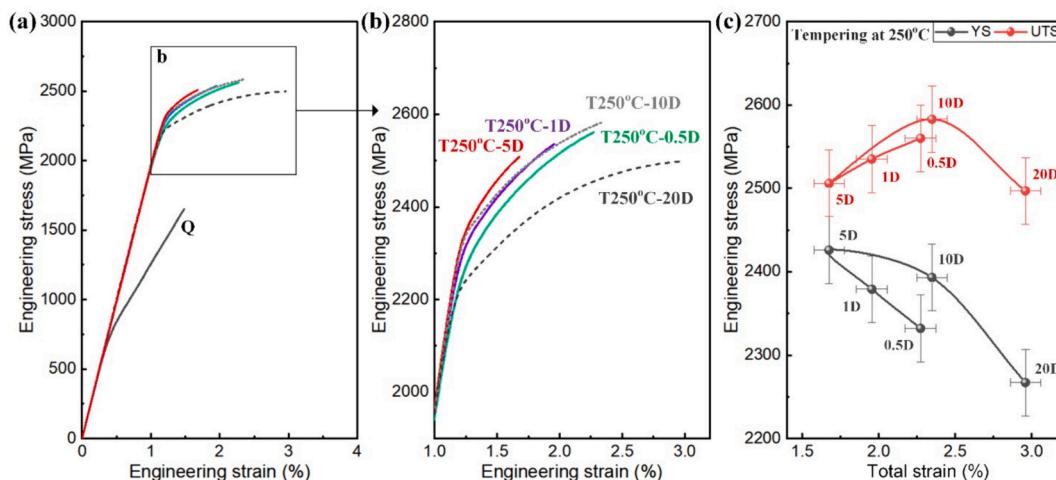


Fig. 1. Schematic diagram of the heat treatment of targeted high-carbon steel.



**Fig. 2.** (a) (b): Engineering stress-strain curves of high-carbon martensite steel after tempering at 175 °C for different periods as indicated. (b) Enlarged view of (a). (c) YS and UTS vs total strain obtained from (a) and (b).



**Fig. 3.** (a) (b): Engineering stress-strain curves of high-carbon martensite steel after tempering at 250 °C for different periods as indicated. (b) Enlarged view of (a). (c) YS and UTS vs total strain obtained from (a) and (b).

Further discussions on the difference in carbon solid solution will be presented in section 4.

Furthermore, micro-hardness and compressive stress-strain curves were collected for different tempered specimens to reflect their

behaviour under compressive stress, a common scenario in practical applications. The corresponding results are presented in Figs. 4a-c. It can be seen that the variation tendency of hardness with increasing tempering time is similar to that of the tensile strength, as mentioned

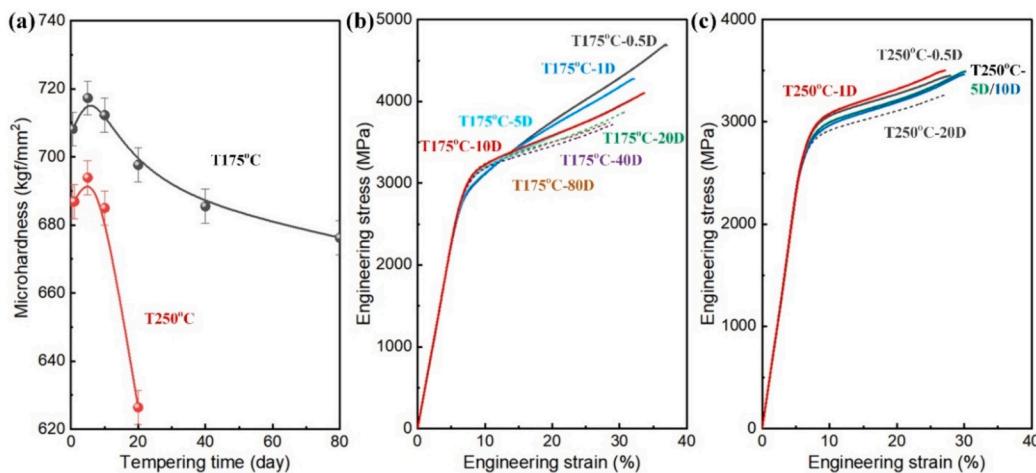


**Fig. 4.** Microhardness (a) and the compressed engineering stress-strain curves (b) (c) of the tempered high-carbon steel at 175 °C and 250 °C for different periods as indicated.

above. However, the obvious difference is that the maximum hardness is obtained in the tempered specimens for about 5 d, as shown in Fig. 4a. Ultralong term tempering results in decreased hardness, with a value of about 680 kgf/mm<sup>2</sup> observed in the tempered specimen at 175 °C and 625 kgf/mm<sup>2</sup> in the tempered specimen at 250 °C.

The compressive stress-strain curves presented in Fig. 4b illustrate that the highest compressed YS of 3200 MPa is achieved in the tempered specimen at 175 °C for a duration of 10 d. However, it should be noted that the short-term tempered specimen for 0.5 d exhibits the maximum ultimate compressed strength of 4800 MPa, with a significantly larger strain hardening rate than that of the long-term tempered specimens for over 10 d. This phenomenon may be attributed to the transformation-induced plasticity (TRIP) effect of a large amount of RA, which provides a substantial hardening contribution. Nonetheless, such an effect may not be significant in the tempered specimens at 250 °C for a prolonged time, as evidenced by the observed maximum compressed YS in the tempered specimen for 1 d, with the value of 3200 MPa, as shown in Fig. 4c.

After an ultralong tempering time, both compressed YS and ultimate strength decrease might be primarily due to the weakening of the carbon solid solution strengthening. Interestingly, the duration of tempering time required to attain maximum compressed YS or hardness is shorter than that for the maximum tensile YS. This may be attributed to the different stress states around movable dislocations, which leads to the difference in the optimum match of precipitation and solid solution strengthening, as discussed elsewhere [4].

### 3.2. Microstructure of martensite and tempered martensite

The SEM image of a quenched specimen, presented in Fig. 5a, displays a typical microstructure consisting of quenched martensite with embedded primary carbides, which is consistent with the conventional microstructure found in bearing steel [27]. In addition, the carbon content in the matrix might have decreased, effectively avoiding forming large-sized martensite plates. To determine the carbon content in the martensite matrix, Fig. 5b shows the extracted morphology of primary carbides with schematic martensite structure, corresponding to the SEM image in Fig. 5a.

The volume fraction of carbides was calculated to be around 0.081, while the carbon content in the martensite matrix was estimated to be 0.5 wt%, based on the conservation of carbon mass. As reported in previous works, the substructure of this type of martensite is known to consist of dislocations and twins, which was simultaneously observed in Fig. 6, showing dislocation martensite (Figs. 6b-d) and twinned martensite (Figs. 6e-g) near each other (Fig. 6a). The crystal defects in the martensite serve as nucleation sites for particle precipitation. Similarly, quenched dislocations and twins can also act as nucleation sites for typical carbides, as observed after low-temperature tempering.

As mentioned above, the mechanical properties of high-carbon

quenched martensite steel can be effectively improved by low-temperature tempering. In this regard, Fig. 7 illustrates the microstructures of specimens subjected to tempering at 175 °C. The results show that ultrafine carbides are uniformly distributed in the martensite matrix. Notably, no significant difference is observed in the carbide morphology and distribution among specimens tempered for different durations, as determined through SEM analysis. Therefore, the present study focuses on the substructure of the specimen exhibiting the highest strength, tempered at 175 °C for 40 d. Fig. 8 presents corresponding TEM results, indicating that typical θ-carbides, Fig. 8d, precipitate around the twin structure (Figs. 8b-c). Similarly, θ-carbides are observed near dislocated martensite (Figs. 8e-f), albeit with an unclear morphology, Fig. 8g.

It is known that increasing tempering temperature can facilitate the precipitation and growth of carbides. This phenomenon is observed in the carbide distribution of specimens tempered at 250 °C, as depicted in Fig. 9. Although the short-term tempered specimen (Fig. 9a) exhibits a slightly lower amount of carbides than the long-term tempered specimens. However, no significant difference in the carbide morphology is observed after tempering for over 1 d (Figs. 9b-e), similar to the tempered specimens at 175 °C. Moreover, the detailed TEM analysis of the strongest tempered specimen at 250 °C for 5 d, presented in Fig. 10, reveals that θ-carbides, Fig. 10a, preferentially precipitate around the location of twins (Figs. 10b-c). While the carbides precipitated in the dislocations are relatively lower, as shown in Figs. 10e-g. It can be inferred that the dislocation density decreases before the nucleation of typical carbides, leading to a lower amount of carbides. Additionally, this implies an increase in the diffusing distance of carbon atoms in the martensite matrix between adjacent carbides.

However, it is worth noting that the carbon content of the tempered martensite matrix is not evident in the martensitic morphology. The invisible carbon solid solution may be crucial in affecting the tensile strength and ductility, which will be discussed in the subsequent section.

### 3.3. Evolution of retained austenite

To investigate the effect of RA on the strength and ductility of the ultralong-term tempered high-carbon steel, detailed XRD analyses were performed on specimens tempered at 175 °C and 250 °C. The results, shown in Figs. 11–12, indicate that the RA content in tempered specimens at 175 °C diminishes with prolonged tempering time, as shown in Fig. 12a. The RA content in the quenched specimen is about 33%, which remains high at about 23% even after tempering for 0.5 d and 1 d. Further RA decomposing leads to a lower content of about 3%. Upon reaching a tempering time of 40 d, RA is hardly detectable, coinciding with the specimen's maximum strength mentioned earlier.

As tempering time increases, a visible left shift of the peak at about 50.75° of RA, especially for specimens tempered for 20 d, as shown in Fig. 11c. This shift indicates lattice broadening resulting from carbon

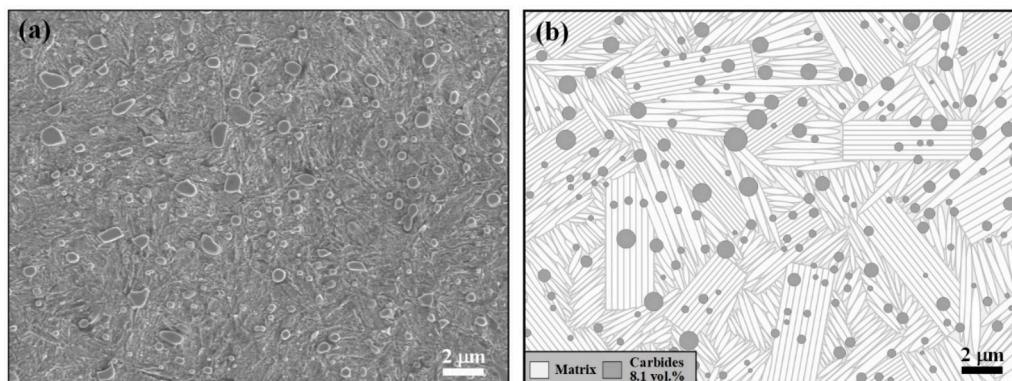


**Fig. 5.** SEM image (a) and primary carbides distribution (b) with schematic martensite structure of high-carbon martensite steel after quenching in oil.

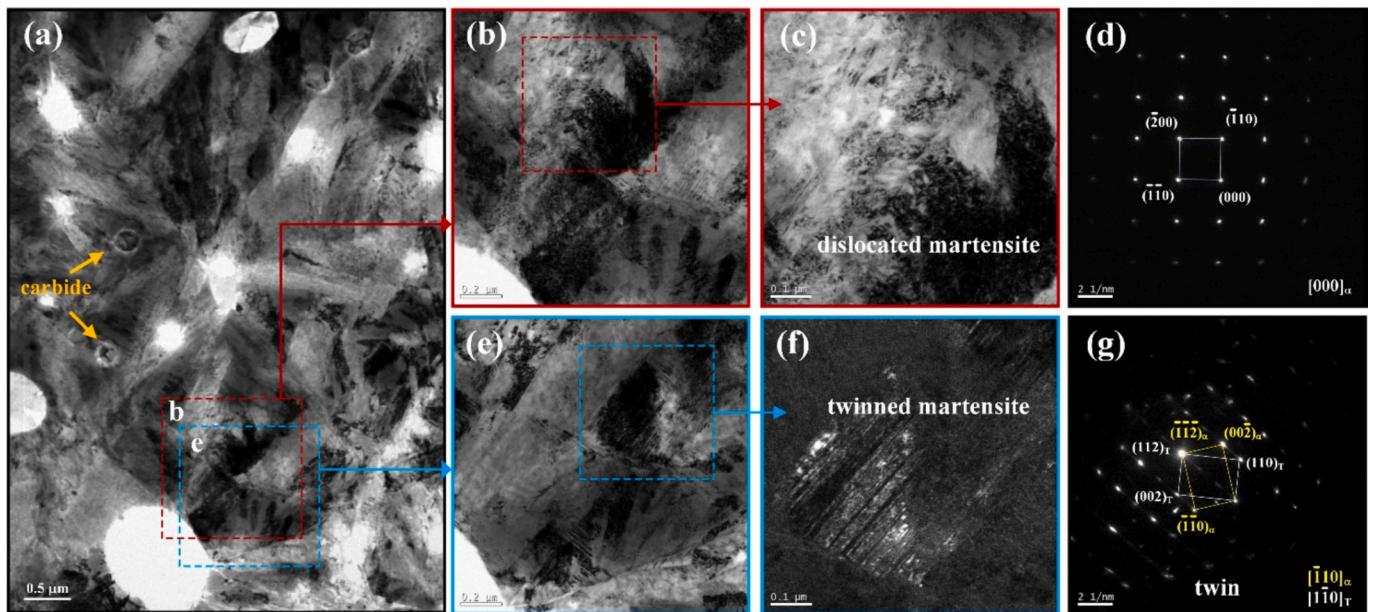


**Fig. 6.** TEM images of high-carbon martensite steel after quenching in oil. (b) and (e) are enlarged views of the area in (a). (c) and (f) are enlarged views of the area in (b) and (e), respectively. (d) and (g) are selected area electron diffractions corresponding with the area in (c) and (f), suggesting dislocated and twinned martensite.

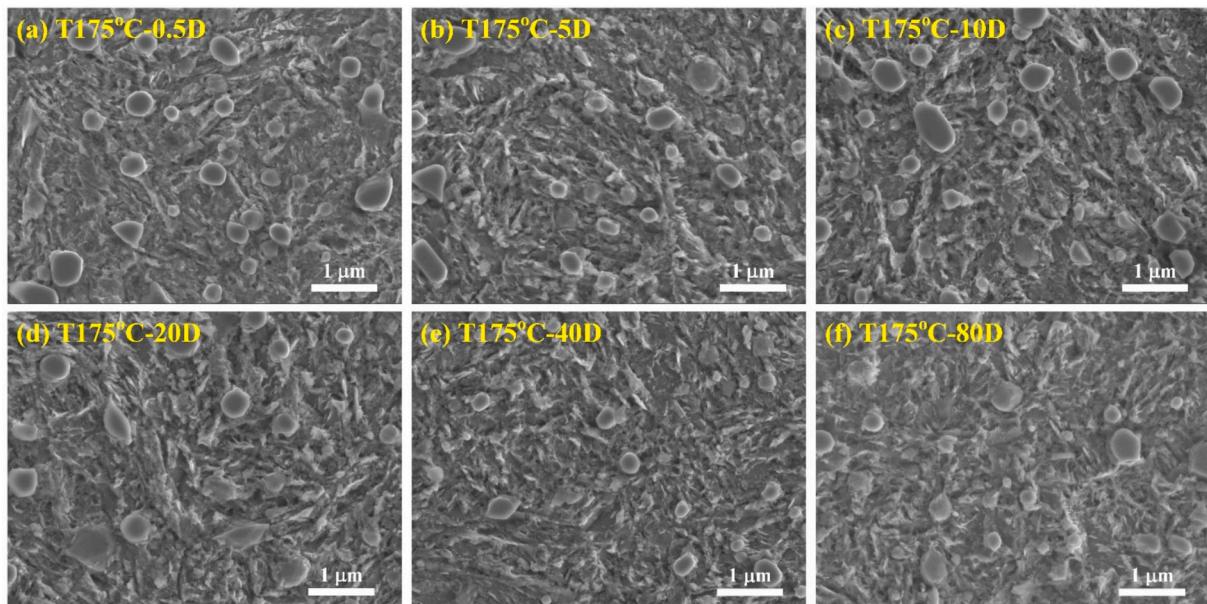


**Fig. 7.** SEM images of high-carbon martensite steel after tempering at 175 °C for different times as indicated.

partitioning from high-carbon martensite matrix to RA. The carbon content ( $C_\gamma$ ) of RA can be calculated using the Eq. [27]:  $a_\gamma = 3.548 + 0.044 \cdot C_\gamma$ , where  $a_\gamma$  is the lattice constant of RA. The detailed values of the carbon content of RA in different specimens are shown in Fig. 12b, with a maximum value of about 1.5 wt% achieved after tempering for 20 d. Based on this, we can also estimate the carbon solid solution strengthening of RA, which is discussed in the following section.

However, a small amount of RA is observed in the tempered specimen at 250 °C, as shown in Fig. 13. Consistent with the strength evolution presented in Fig. 3, RA has rapidly decomposed after short-term tempering at 250 °C, even for 0.5 d. Thus, the effect of RA on the strength and ductility can be disregarded for tempered specimens at 250 °C.

#### 4. Discussion

##### 4.1. Typical carbides precipitate and attenuation of carbon solid solution

As mentioned above, the typical carbides will precipitate in the tempered martensite matrix after tempering at 175 °C and 250 °C. The precipitate strengthening of typical carbides should be considered in the total strengthening mechanism of the ultralong-term tempered high-carbon steel. Thus, it is necessary to clarify the growth of the carbides with increasing tempering time, especially for their diameter  $d_c$  and volume fraction  $f$ . This kind of precipitation is subjected to the diffusion of carbon atoms in the martensite matrix, and accordingly, the growth rate can be expressed by the following Eq. (1):

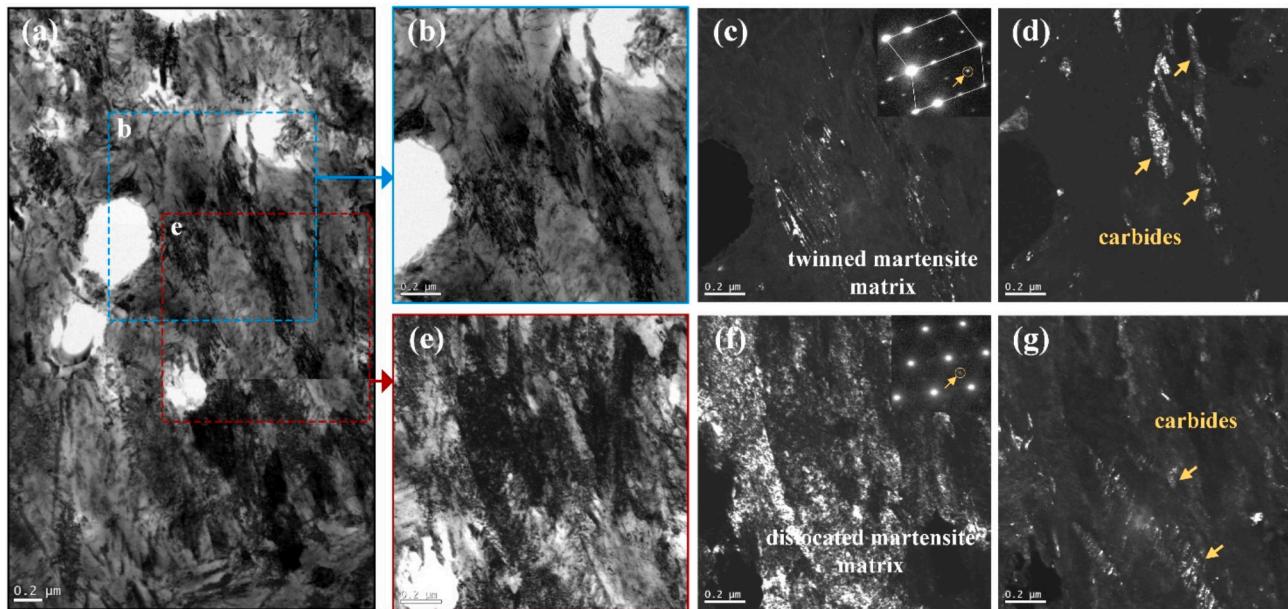


**Fig. 8.** TEM images of high-carbon martensite steel after tempering at 175 °C for 40 d. (b) and (e) are enlarged views of the area in (a). (c-d) and (f-g) are the dark field images of (b) and (e), respectively. The selected area electron diffractions are added in (c) and (f).

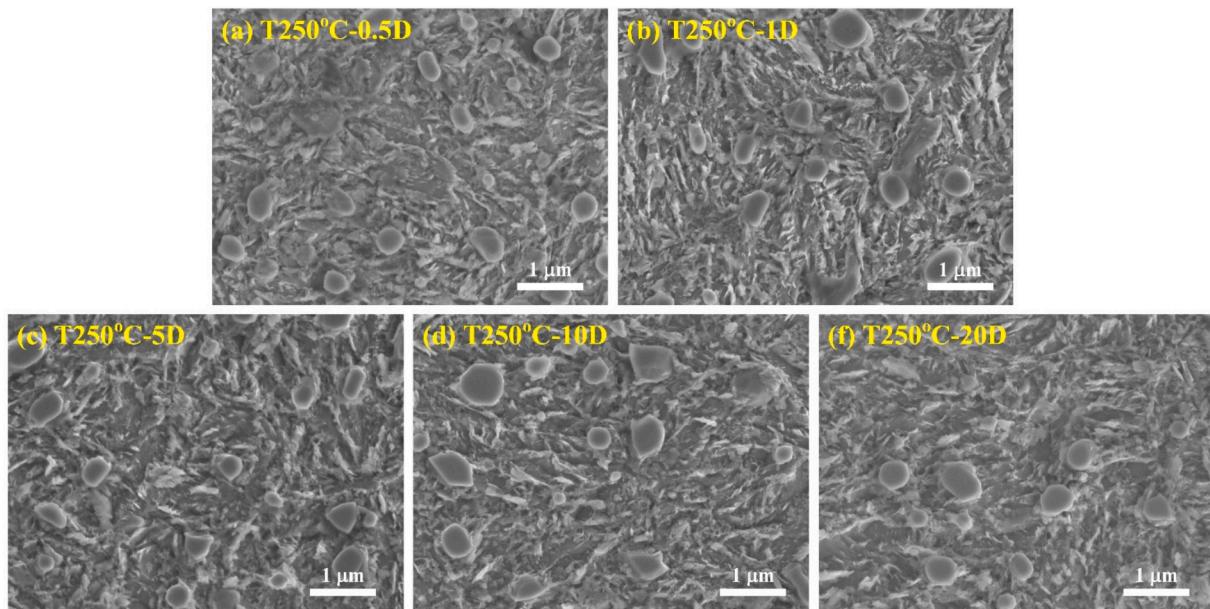


**Fig. 9.** SEM images of high-carbon martensite steel after tempering at 250 °C for different times as indicated.

$$\frac{dr}{dt} = \frac{DC_0}{rC_c}, \quad (1)$$

where  $r$  is the radius of typical carbides,  $t$  is tempering time,  $C_0 = 0.5$  wt % and  $C_c = 6.67$  wt% are the carbon content of the original martensite matrix and the  $\theta$ -carbides, respectively. The initial stages with the transition carbides can be ignored during the calculation of the carbide growth, because of its short duration of only several hours [1].  $D$  is the diffusion coefficient of carbon atoms in the tempered matrix, which can be calculated by the Arrhenius Eq. [28]:  $D=D_0 \exp(-Q/RT)$ .  $D_0 = 2 \times 10^{-5} \text{ m}^2/\text{s}$  is a pre-exponential factor for carbon in a tempered martensite matrix.  $R$  is the gas constant, and  $T$  is the thermodynamic temperature.  $Q$  is the activation energy, defined as 141 kJ/mol here, considering the carbon capture of different defects in a quenched

martensitic matrix.

It should be noted that the well-known Fick's law, expressed by Eq. (2), has been used in the derivation of Eq. (1).

$$\frac{\partial C}{\partial t} = D \frac{\partial^2 C_M}{\partial x^2}, \quad (2)$$

where  $C_M$  is real-time carbon content in the matrix, and  $x$  is the position between adjacent carbides. Here, the mean spacing between adjacent carbides  $L$  can be defined as 120 nm and 560 nm in tempered martensite matrix at 175 °C and 250 °C, respectively, as obtained through the microstructural analysis as mentioned above and  $L = 4r/3f$  from [29].

Meanwhile, based on the diffusion Eq. (2), the weakening of the carbon solid solution can be easily evaluated. As the tempering time surpasses zero, carbon content becomes zero at the position of zero or  $L$ ,

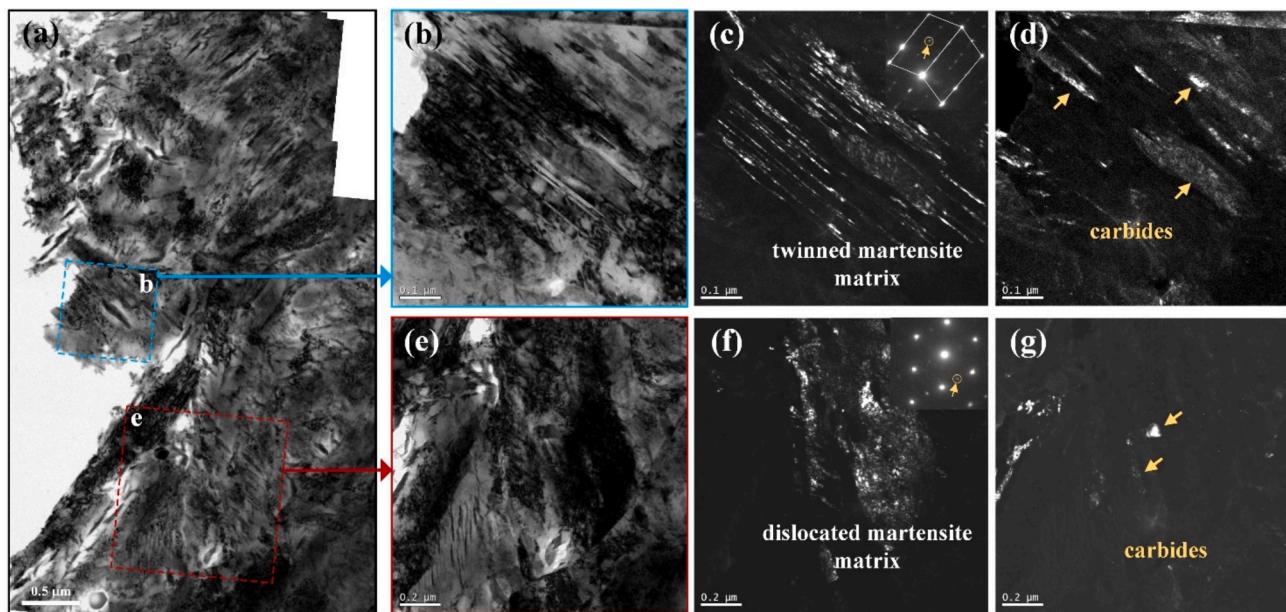


**Fig. 10.** TEM images of high-carbon martensite steel after tempering at 250 °C for 5 d. (b) and (e) are enlarged views of the area in (a). (c-d) and (f-g) are the dark field images of (b) and (e), respectively. The selected area electron diffractions are added in (c) and (f).

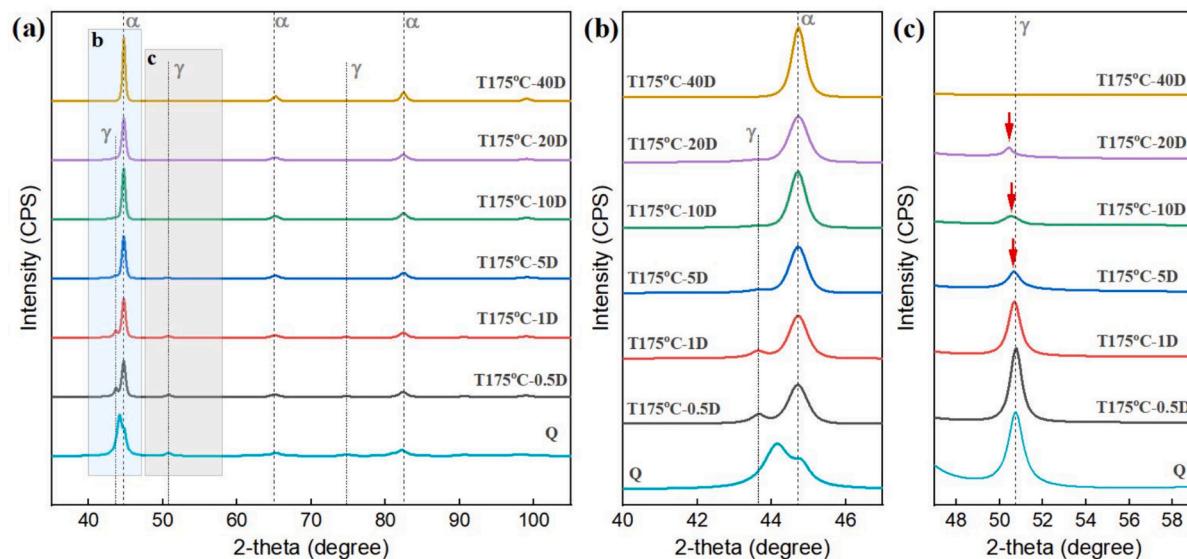


**Fig. 11.** (a): XRD results of high-carbon martensite steel after tempering at 175 °C for different times as indicated. (b) and (c) are the enlarged view of (a).

that is,  $x = 0$  or  $x = L$ . Therefore, the function of carbon content as a function of diffusing distance can be expressed by the following Eq. (3):

$$C_M = \frac{4C_0}{\pi} \sum_{n=0}^{\infty} \frac{1}{2n+1} \sin \frac{(2n+1)\pi x}{L} \exp \left[ \frac{-(2n+1)^2 \pi^2 D t}{L^2} \right]. \quad (3)$$

Based on the above equations, the approximate values of diameter and volume fraction of carbides with increasing tempering time are shown in Table 1. The maximum carbide diameter is about 130 nm for the tempered condition at 250 °C. In contrast, for tempered specimens at 175 °C, the carbide diameters are all found to be below 100 nm. Meanwhile, the evolutions of carbon content in the martensite matrix are shown in Fig. 14. A clear gradient distribution is observed by the diffusion law, as shown in Figs. 14a and 14c. In the adjacent area around carbides, the carbon content is indeed much lower than that in the middle position. The attenuation of carbon content in specimens

tempered at 250 °C is greater than in those tempered specimens at 175 °C. The change of average carbon content in tempered martensite matrix, as shown in Figs. 14b and 14d also show a lower carbon content after tempering at 250 °C. Further, the solid solution strengthening contribution can be assessed based on the average carbon content, which will be discussed in next section.

#### 4.2. Strengthening mechanism

This study has demonstrated exceptional mechanical properties via ultralong-term tempering, particularly UTS exceeding 2.7 GPa UTS in high-carbon steel tempered at 175 °C for 40 and 80 d. And the mechanical properties evolution can be controlled by adjusting tempering time. To investigate the detailed strengthening mechanism at different tempered stages, this study focused on the changes in precipitation strengthening, solid solution strengthening, and dislocations

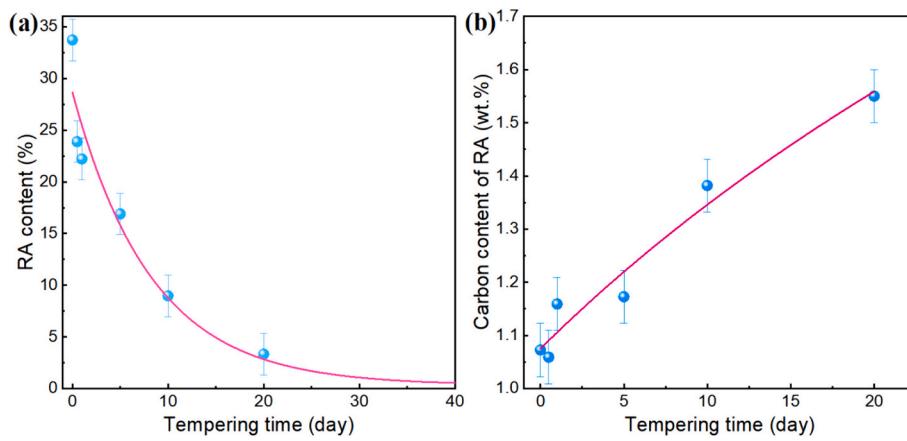


Fig. 12. The RA content (a) and carbon content in RA (b) of high-carbon martensite steel after tempering at 175 °C for different times as indicated.

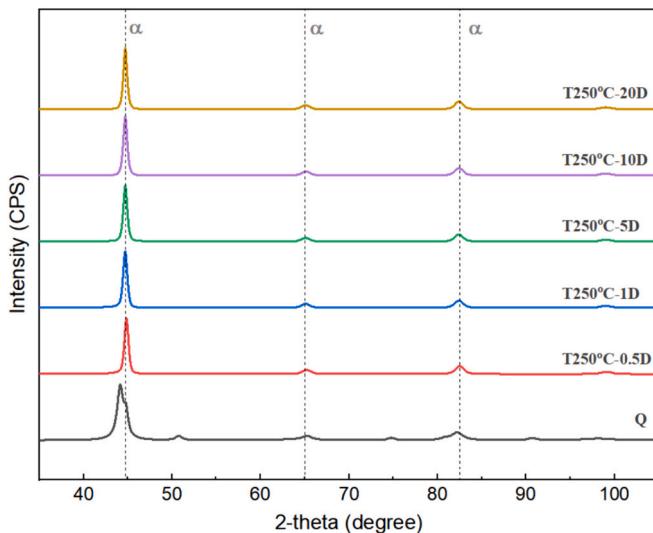


Fig. 13. XRD results of high-carbon martensite steel after tempering at 250 °C for different times as indicated.

strengthening, which are influenced by the tempering holding time. There is no significant difference in the grain boundary, so grain refinement strengthening remains constant. However, it is essential to consider the contribution of the softer RA. Therefore, the YS can be expressed simply as the following Eq. (4) [6]:

$$YS = (1 - f') \cdot \left( \sigma_{ss}^M + \sigma_{dis}^M + \sigma_p + K_M d^{1/2} \right) + f' \left( \sigma_{ss}' + K_\gamma d^{1/2} \right), \quad (4)$$

where  $f'$  is RA content, of which the value is obtained from XRD analysis as illustrated in Fig. 12a.  $\sigma_{ss}^M$ ,  $\sigma_{ss}'$ ,  $\sigma_{dis}^M$ ,  $\sigma_p$ , and  $K_M d^{1/2}$ ,  $K_\gamma d^{1/2}$  are the strengthening contribution from solid solution, precipitation, dislocations and grain boundary for tempered martensite and RA, respectively. Here,  $K_M = 112 \text{ MPa } \mu\text{m}^{1/2}$  [30] and  $K_\gamma = 370 \text{ MPa } \mu\text{m}^{1/2}$  [31] are constant in the Hall-Petch relationship. The values were selected based on the effective grain size of martensite and austenite, respectively. The

effect of the difference in alloy content can be ignored because it mainly changes the constant term in the Hall-Petch relationship. Considering the martensite plate has a needle-like morphology, its length is indeed longer than several micrometres while the width is smaller, approximately 100–200 nm. And because of the disordered orientation of the plate, we estimated the grain size using an average value of about 1 μm. For solid solution strengthening,  $\sigma_{ss}^M$  and  $\sigma_{ss}'$  can be expressed as  $\sigma_{ss}^M = k_M C_M$  and  $\sigma_{ss}' = k_\gamma C_\gamma$ .  $k_M$  was obtained by fitting previous experimental results [32,33], for fully martensitic steels.  $k_\gamma$  is defined as 187 MPa·(wt %)<sup>-1</sup> [34,35]. The solid strengthening of the matrix is also heterogeneous, due to the gradient carbon distribution as shown in Figs. 14a and 14c. However, the solid solution strengthening has a linear increasing relationship with carbon content. Thus, an average carbon content was used to estimate carbon solid solution strengthening. The Taylor hardening formula is used to evaluate the dislocation strengthening [36]:  $\sigma_{dis}^M = MaGb\rho^{1/2}$ , where, Taylor factor  $M = 3$ , constant  $\alpha = 0.25$ , shear modulus  $G = 80 \text{ GPa}$  and Burgers vector  $b = 0.248 \text{ nm}$  for tempered martensite matrix. However, the dislocation density  $\rho$  can be considered as a function of the carbon content of tempered martensite matrix [36]:  $\rho = (0.7 + 3.5 \times C_M) \times 10^{15}$ .

For precipitation strengthening of typical carbides, the shearing through and bypassed mechanisms [29] are used in this study to explain the dislocation slipping around the typical carbides in small and large sizes, respectively. Here, the applied matrix phase was tempered martensite with a body-centred cubic structure. And the value of shearing through strengthening can be evaluated by the equation:  $\sigma_p^s = 0.28\sigma_A^{3/2}f^{1/3}b^2\sqrt{r}/\sqrt{G}$ , where  $\sigma_A$  is the antiphase boundary energy. Here, the value of  $\sigma_A$  is defined as about  $350 \times 10^{-7} \text{ J/cm}^2$  and  $525 \times 10^{-7} \text{ J/cm}^2$  and for carbides in tempered specimens at 175 °C and 250 °C, respectively, which might be due to different types of carbides. The bypassed mechanism can be described using the classical Orowan relationship:  $\sigma_p^b = 0.538Gb d_c^{-1}\sqrt{f ln(\frac{d_c}{2b})}$ . It should be noted that the precipitation strengthening in the tempered specimen at 175 °C can be just evaluated by shearing through mechanism due to its smaller particle size, as shown in Table 1. However, both two mechanisms could be applied to the tempered specimen at 250 °C, considering an obvious increasing diameter from about 20 nm to 130 nm or more. To evaluate

Table 1

The calculated value of diameter and volume fraction of carbides with increasing tempering time.

Tempering time	0.5 D	1 D	5 D	10 D	20 D	40 D	80 D
T175°C	$d_c$ (nm)	2.42	2.78	4.76	6.43	8.88	12.40
	$f$ (%)	1.35	1.55	2.65	3.58	4.94	6.89
T250°C	$d_c$ (nm)	20.75	29.28	65.36	92.41	130.68	—
	$f$ (%)	2.47	3.48	7.78	11.00	15.56	—

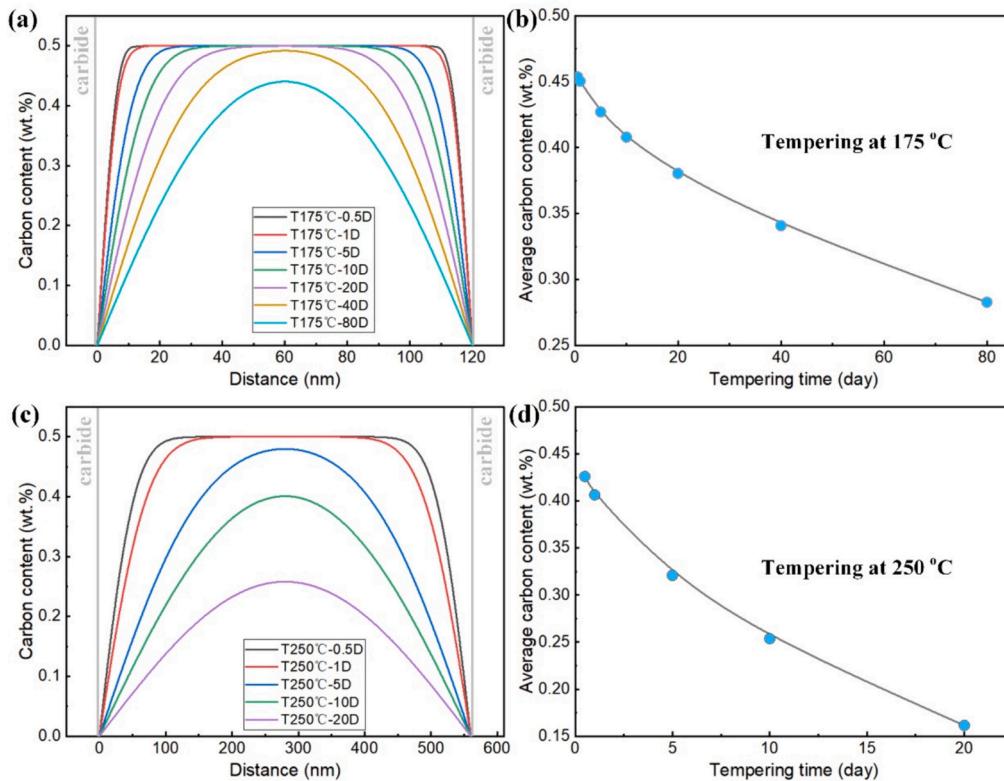


**Fig. 14.** (a) (b): The calculated carbon content of tempered martensite matrix between adjacent carbides for tempering at 175 °C and 250 °C. (b) and (d) are average carbon content corresponding with (a) and (c).

the corresponding precipitation strengthening, a proportionality coefficient:  $k_p^s = \exp\left(\frac{t}{1 \times 10^7}\right) - 1$ , is introduced, and its value can be expressed by  $\sigma_p = (1 - k_p^s)\sigma_p^s + k_p^s\sigma_p^b$ .

In summary, the calculated strengthening contribution of solid solution, dislocations, precipitation and RA are shown in Figs. 15a and 15c. The variation of total calculated YS is consistent with the experimental values for the tempered specimens at 175 °C and 250 °C (in

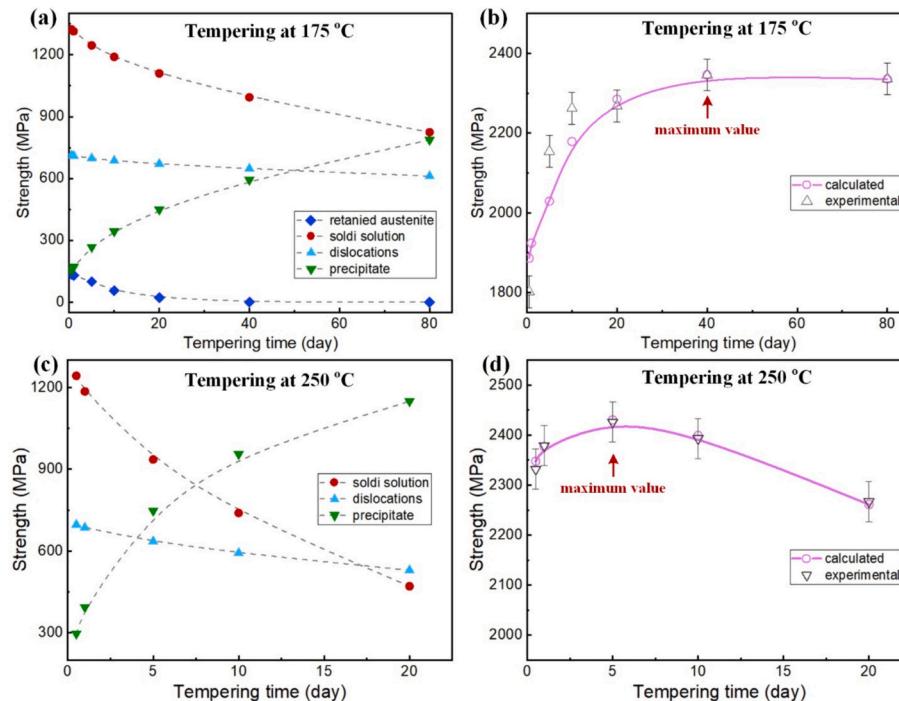


**Fig. 15.** (a) (b): The calculated strengthening contribution of solid solution, dislocations, precipitation and RA for tempered specimens at 175 °C and 250 °C. (b) and (d) are the corresponding total calculated YS compared to the experimental values.

Figs. 15b and 15d). It can be seen that the primary strengthening mechanism in the initial stage of ultralong-term tempering is carbon solid solution strengthening with a value exceeding 1000 MPa. As the tempering time increases, solid solution and dislocations strengthening weaken, whereas the precipitation strengthening increases with the growth and volume fraction increasing of carbides. The mixtures of these three strengthening mechanisms result in an initial increase and a subsequent decrease in the total YS after ultra-long tempering. However, the effect of RA must be noticed in the tempered specimens at 175 °C, especially for the softer value of about 150 MPa in the initial stage. The corresponding TRIP also provides a partly hardening effect and ductility.

## 5. Conclusion

To further investigate the microstructural evolution and develop optimum mechanical properties of the conventional high-carbon martensitic steel, ultralong-term tempering was carried out at a lower temperature of about 175 °C and 250 °C. Several primary conclusions are summarized below:

- (1) An excellent mechanical property has been obtained, showing 2.7 GPa UTS, 2.3 GPa YS and good ductility after ultralong-term tempering at 175 °C for over 40 d. Additionally, the specimens tempered at 250 °C for 5 d exhibits an ultrahigh YS value exceeding 2.4 GPa. Furthermore, it shows an increased tendency of YS in the initial stage followed by a decreased tendency with increasing ultra-long holding time of high-carbon steel specimens tempered at 175 °C and 250 °C.
- (2) The main phases of ultralong-term tempered high-carbon steel were characterized as the typical tempered martensite matrix embedded by ultrafine carbides. The residual austenite (RA) decomposed slowly with increasing tempering time at 175 °C, leading to a significant increase in strength. However, RA has no pronounced effect on the strength evolution for specimens tempered at 250 °C. Typical carbides were found to nucleate at quenched crystal defects and grow with increasing holding time while the carbon content in the martensite matrix decreased.
- (3) The primary strengthening mechanism during the initial stage of ultralong-term tempering was carbon solid solution strengthening, with a value exceeding 1000 MPa. The solid solution strengthening effect is weakened with increasing tempering holding time, while precipitation strengthening increases with the growth and volume fraction of carbides. The combined effect of solid solution, dislocations, precipitation strengthening contributions and the softening of retained austenite resulted in a total yield strength curve that increased initially, followed by a decrease with ultralong-term holding time of high-carbon steel specimens tempered at 175 °C and 250 °C.

## CRediT authorship contribution statement

**Jian Wang:** Writing – review & editing, Writing – original draft, Visualization, Validation, Software, Methodology, Investigation, Funding acquisition, Conceptualization. **G.M.A.M. El-Fallah:** Writing – review & editing, Visualization, Validation, Supervision, Methodology, Investigation. **Xiangdong Chang:** Visualization, Resources, Project administration. **Yuxing Peng:** Visualization, Resources, Project administration. **Qing Tao:** Writing – review & editing, Writing – original draft, Visualization, Supervision, Resources, Methodology, Investigation, Funding acquisition, Formal analysis, Conceptualization.

## Declaration of competing interest

The authors declare that they have no known competing financial interests or personal relationships that could have appeared to influence the work reported in this paper.

## Data availability

Data will be made available on request.

## Acknowledgement

The authors would like to express their special acknowledgement to Prof Sir H. K. D. H. Bhadeshia for his insightful and constructive comments on this paper. This work was financially supported by the National Natural Science Foundation of China (Grant Nos. 51805533 and 51641109).

## References

- [1] A.T.W. Barrow, J.H. Kang, P.E.J. Rivera-Díaz-del-Castillo, The  $\epsilon \rightarrow \eta \rightarrow \theta$  transition in 100Cr6 and its effect on mechanical properties, *Acta Mater.* 60 (6) (2012) 2805–2815.
- [2] K. Chen, Z. Jiang, F. Liu, J. Yu, Y. Li, W. Gong, C. Chen, Effect of quenching and tempering temperature on microstructure and tensile properties of microalloyed ultra-high strength suspension spring steel, *Mater. Sci. Eng. A* 766 (2019) 138272.
- [3] H. Bhadeshia, R. Honeycombe, *Steels: Microstructure and Properties*, Butterworth-Heinemann, 2017.
- [4] H.K.D.H. Bhadeshia, *Steels for bearings*, *Prog. Mater. Sci.* 57 (2) (2012) 268–435.
- [5] G. Krauss, Deformation and fracture in martensitic carbon steels tempered at low temperatures, *Mater. Trans. B Process Metall. Mater. Process. Sci.* 32 (2) (2001) 205–221.
- [6] E.I. Galindo-Nava, P.E.J. Rivera-Díaz-del-Castillo, Understanding the factors controlling the hardness in martensitic steels, *Scr. Mater.* 110 (2016) 96–100.
- [7] S. Murphy, A. Whiteman, The precipitation of epsilon-carbide in twinned martensite, *Metall. Trans. A* 1 (4) (1970) 843–848.
- [8] W. Song, J. von Appen, P. Choi, R. Dronskowski, D. Raabe, W. Bleck, Atomic-scale investigation of  $\epsilon$  and  $\theta$  precipitates in bainite in 100Cr6 bearing steel by atom probe tomography and ab initio calculations, *Acta Mater.* 61 (20) (2013) 7582–7590.
- [9] Q. Tao, J. Wang, E.I. Galindo-Nava, Effect of low-temperature tempering on confined precipitation and mechanical properties of carburised steels, *Mater. Sci. Eng. A* 822 (2021) 141688.
- [10] Y. Ohmori, S. Sugisawa, The precipitation of carbides during tempering of high carbon Martensite, *Trans. Jpn. Inst. Metals* 12 (3) (1971) 170–178.
- [11] R.L. Banerjee, X-ray determination of retained austenite, *J. Heat Treat.* 2 (2) (1981) 147–150.
- [12] P.W. Mason, P.S. Prevéy, Iterative taguchi analysis: optimizing the austenite content and hardness in 52100 steel, *J. Mater. Eng. Perform.* 10 (1) (2001) 14–21.
- [13] J.M. Beswick, Fracture and fatigue crack propagation properties of hardened 52100 steel, *Mater. Trans. A* 20 (10) (1989) 1961–1973.
- [14] J. Wang, Q. Tao, H. Zheng, L. Fu, A. Shan, Microstructure and mechanical properties of a continuous carbon-gradient sheet steel, *Mater. Lett.* 308 (2022) 131059.
- [15] A.J. Clarke, M.K. Miller, R.D. Field, D.R. Coughlin, P.J. Gibbs, K.D. Clarke, D. J. Alexander, K.A. Powers, P.A. Papin, G. Krauss, Atomic and nanoscale chemical and structural changes in quenched and tempered 4340 steel, *Acta Mater.* 77 (2014) 17–27.
- [16] H.K.D.H. Bhadeshia, A.R. Chintha, S. Lenka, Critical assessment 34: are  $\gamma$  (Hägg),  $\eta$  and  $\epsilon$  carbides transition-phases relative to cementite in steels? *Mater. Sci. Technol.* 35 (11) (2019) 1301–1305.
- [17] B.P.J. Sandvik, C.M. Wayman, Direct observations of carbon clusters in a high-carbon martensitic steel, *Metallography* 16 (4) (1983) 429–447.
- [18] E.I. Galindo-Nava, P.E.J. Rivera-Díaz-del-Castillo, A model for the microstructure behaviour and strength evolution in lath martensite, *Acta Mater.* 98 (2015) 81–93.
- [19] J. Zhang, Z. Dai, L. Zeng, X. Zuo, J. Wan, Y. Rong, N. Chen, J. Lu, H. Chen, Revealing carbide precipitation effects and their mechanisms during quenching-partitioning-tempering of a high carbon steel: experiments and modeling, *Acta Mater.* 217 (2021) 117176.
- [20] E.S. Alley, R.W. Neu, Microstructure-sensitive modeling of rolling contact fatigue, *Int. J. Fatigue* 32 (5) (2010) 841–850.
- [21] W. Cui, M. Gintalas, P.E.J. Rivera-Díaz-del-Castillo, Stability of retained austenite in martensitic high carbon steels, Part II: Mechan. Stabilit., *Mater. Sci. Eng.: A* 711 (2018) 696–703.
- [22] W. Cui, D. San-Martín, P.E.J. Rivera-Díaz-del-Castillo, Stability of retained austenite in martensitic high carbon steels, Part I: Therm. Stabilit., *Mater. Sci. Eng.: A* 711 (2018) 683–695.
- [23] S. Qin, Y. Liu, Q. Hao, Y. Wang, N. Chen, X. Zuo, Y. Rong, The mechanism of high ductility for novel high-carbon quenching-partitioning-tempering martensitic steel, *Metall. Mater. Trans. A* 46 (9) (2015) 4047–4055.
- [24] S. Qin, Y. Liu, Q. Hao, Y. Wang, N. Chen, X. Zuo, Y. Rong, High carbon microalloyed martensitic steel with ultrahigh strength-ductility, *Mater. Sci. Eng. A* 663 (2016) 151–156.
- [25] S. Qin, Y. Liu, Q. Hao, X. Zuo, Y. Rong, N. Chen, Ultrahigh ductility, high-carbon martensitic steel, *Metall. Mater. Trans. A* 47 (10) (2016) 4853–4861.
- [26] J. Speer, D.K. Matlock, B.C. De Cooman, J.G. Schroth, Carbon partitioning into austenite after martensite transformation, *Acta Mater.* 51 (9) (2003) 2611–2622.

- [27] C.S. Roberts, Effect of carbon on the volume fractions and lattice parameters of retained austenite and Martensite, *JOM* 5 (2) (1953) 203–204.
- [28] Q. Tao, J. Wang, L. Fu, Z. Chen, C. Shen, D. Zhang, Z. Sun, Ultrahigh hardness of carbon steel surface realized by novel solid carburizing with rapid diffusion of carbon nanostructures, *J. Mater. Sci. Technol.* 33 (10) (2017) 1210–1218.
- [29] T. Gladman, Precipitation hardening in metals, *Mater. Sci. Technol.* 15 (1) (1999) 30–36.
- [30] C. Zhang, Q. Wang, J. Ren, R. Li, M. Wang, F. Zhang, K. Sun, Effect of martensitic morphology on mechanical properties of an as-quenched and tempered 25CrMo48V steel, *Mater. Sci. Eng. A* 534 (2012) 339–346.
- [31] Z. Yanushkevich, S.V. Dobatkin, A. Belyakov, R. Kaibyshev, Hall-Petch relationship for austenitic stainless steels processed by large strain warm rolling, *Acta Mater.* 136 (2017) 39–48.
- [32] A. Litwinchuk, F.X. Kayser, H.H. Baker, A. Henkin, The Rockwell C hardness of quenched high-purity iron-carbon alloys containing 0.09 to 1.91% carbon, *J. Mater. Sci.* 11 (7) (1976) 1200–1206.
- [33] R.A. Grange, C.R. Hribal, L.F. Porter, Hardness of tempered martensite in carbon and low-alloy steels, *Metall. Trans. A*. 8 (11) (1977) 1775–1785.
- [34] O. Bouaziz, H. Zurob, B. Chehab, J.D. Embury, S. Allain, M. Huang, Effect of chemical composition on work hardening of Fe—Mn—C TWIP steels, *Mater. Sci. Technol.* 27 (3) (2011) 707–709.
- [35] J.-B. Seol, J.E. Jung, Y.W. Jang, C.G. Park, Influence of carbon content on the microstructure, martensitic transformation and mechanical properties in austenite/ $\epsilon$ -martensite dual-phase Fe–Mn–C steels, *Acta Mater.* 61 (2) (2013) 558–578.
- [36] Y. Wang, J. Sun, T. Jiang, Y. Sun, S. Guo, Y. Liu, A low-alloy high-carbon martensite steel with 2.6 GPa tensile strength and good ductility, *Acta Mater.* 158 (2018) 247–256.